Spin-Polarization Transfer in Colloidal Magnetic-Plasmonic Au/Iron Oxide Hetero-nanocrystals

Francesco Pineider,[×,‡] César de Julián Fernández,[†,‡,*] Valeria Videtta,[§] Elvio Carlino,[⊥] Awni al Hourani,[#] Fabrice Wilhelm,[▽] Andrei Rogalev,[▽] P. Davide Cozzoli,[§,¶] Paolo Ghigna,[○,*] and Claudio Sangregorio[†,‡]

[×]C.N.R.—I.S.T.M. c/o Dipartimento di Scienze Chimiche, Università di Padova and INSTM, Via Marzolo 1, I-35131, Padova, Italy, [†]C.N.R.—I.S.T.M. Via C. Golgi 19, I-20133 Milano, Italy, [‡]INSTM and Dipartimento di Chimica "U. Schiff", Università degli Studi di Firenze, Via della Lastruccia 3, Sesto Fiorentino, I-50019 Firenze, Italy, [§]National Nanotechnology Laboratory (NNL), CNR Istituto Nanoscienze, c/o Distretto Tecnologico, Via per Arnesano km 5, I-73100 Lecce, Italy, [⊥]TASC National Laboratory, IOM-CNR, Area Science Park, Basovizza, Building MM, SS 14, Km 163.5, I-34149 Trieste, Italy, [#]INSTM and Dipartimento di Fisica "A. Volta", Università di Pavia, Via Bassi 4, I-27100 Pavia, Italy, [▽]European Synchrotron Radiation Facility (ESRF), BP-220, F38043, Grenoble, France, [¶]INSTM and Dipartimento di Matematica e Fisica "E. De Giorgi", Università del Salento, Via per Arnesano, I-73100 Lecce, Italy, and [○]INSTM and Dipartimento di Chimica, Università di Pavia, Viale Taramelli 16, I-27100 Pavia, Italy

ABSTRACT We report on the unprecedented direct observation of spin-polarization transfer across colloidal magneto-plasmonic Au@Fe-oxide core@shell nanocrystal heterostructures. A magnetic moment is induced into the Au domain when the magnetic shell contains a reduced Fe-oxide phase in direct contact with the noble metal. An increased hole density in the Au states suggested occurrence of a charge-transfer process concomitant to the magnetization transfer. The angular to spin magnetic moment ratio, m_{orb}/m_{spin}, for the Au 5d states, which was found to be equal to 0.38, appeared to be unusually large when compared to previous findings. A mechanism relying on direct hybridization between the Au and Fe states at the core/shell interface is proposed to account for the observed transfer of the magnetic moment.

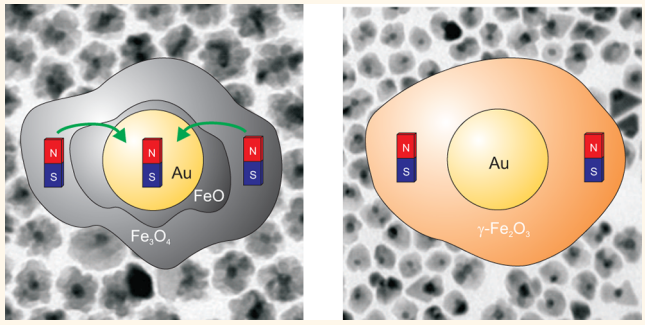

KEYWORDS: colloidal nanocrystals · core−shell heterostructures · spin polarization · X-ray spectroscopy · nanomagnetism · magneto-plasmonics

The combination of nanostructured materials exhibiting different physical properties is one of the key goals in the current landscape of nanotechnology in the perspective of gaining a deeper fundamental understanding of nanoscale phenomena as well as of paving the way toward new exciting applications.[1−4] In particular significant research efforts have been devoted to the design and fabrication of artificial magnetic-plasmonic nanoheterostructures (MP-NHs), in the form of free-standing multicomponent nanocrystals or thin-film multilayers composed of surface plasmon resonance (SPR)-active noble-metal and magnetic domains in direct electronic contact through bonding (*e.g.*, epitaxial) interfaces.[2,3,5,6] MP-NHs have already been proposed as multifunctional platforms for a variety of applications. Most examples pertain the exploitation of MP-NHs with core@shell geometries in theranostics, whereby a noble-metal shell can serve to protect an underlying magnetic core against oxidation,[6,7] to provide a surface easy to functionalize with biomolecules,[8−10] to enable optical tracking,[11,12] to act as an optical heater,[13] or as an active optical beacon.[14] Most notably, besides entailing different optical, electromagnetic, and magnetic responses associated with the respective material components, MP-NHs have been found to exhibit additional or even entirely novel properties as a result of the combination and synergistic interactions between the relevant SPR and the magnetic functionalities.[2,3,5,6,15−31] For instance, the spectral SPR response of the noble-metal domains can be appreciably modified upon formation of direct bonding junctions with magnetic sections.[2,3,18,20] In

* Address correspondence to paolo.ghigna@unipv.it, cesar.dejulian@unifi.it.

Received for review July 27, 2012 and accepted December 18, 2012.

Published online December 18, 2012
10.1021/nn305459m

colloidal Au/iron oxide MP-NHs the occurrence of charge transfer,[16,21,22] changes in the local dielectric environment, or spill-out of electron density[29,31] at the interface have been proposed to explain alterations in steady-state optical absorption and ultrafast electron dynamics, enhanced catalytic activity,[21,22] as well as slight modifications in the magnetic behavior,[32,33] as compared to those found for the isolated materials. Enhanced magneto-optical signals have been reported for several noble-metal/ferrite MP-NHs and attributed to optical amplification produced by the giant electromagnetic field associated with the SPR in the plasmonic neighbor.[3,5,15,17,23,26,27,30] A strong interplay between SPR and magnetic properties has been shown to lead to the insurgence of exclusive phenomena, such as magnetic-field-driven modulation of the SPR,[24,28] bleaching of SPR dynamics,[29,31] and plasmon-driven modification of the magnetization reversal process.[25] However, the detailed origin of such effects is still under debate and their understanding poses the challenge of deciphering the relationships between structural-compositional features and the mechanisms of coupling of magnetic and SPR properties in these MP-NHs. One key issue is to discriminate between systems in which the SPR and magnetic components behave additively or synergistically. In this respect, of paramount importance is to understand the degree of interaction between the valence-band electrons of the respective materials, since these dictate both the optical properties of the noble metal and the magnetic behavior of the magnetic domain. A direct signature of this interaction would be the presence of a magnetic moment on the nonmagnetic plasmonic counterpart.

Bulk Au is essentially a diamagnetic material, although the observation of underlying Pauli and orbital paramagnetism has been recently reported.[34] As such, Au cannot manifest any spin polarization resulting from an unbalancing between spin-up and spin-down states. However, in alloys and multilayers involving magnetic metals, hybridization of the valence band may be expected, leading to spin-polarization transfer, as indeed observed in Au−Co multilayers,[35,36] bulk Au−Fe alloys,[37] as well as in Au−Fe alloy nanoparticles.[38] As a major drawback, the chemical instability of ferromagnetic metals calls for alternative materials capable of showing increased resistance against environmental aggression while maintaining satisfactory magnetic properties. Among the most promising candidates within this respect are transition-metal oxides, such as ferrites. Several strategies to prepare magneto-plasmonic Au/Ag adducts with transition metal oxides have recently been documented in the literature. In particular, colloidal chemistry routes have proven to be extremely versatile, giving access to a wide variety of heterostructured nanocrystals with different architectures and spatial distribution of their chemical composition.[2,39] Currently, there is an undoubtedly huge scope on extending the current understanding of magneto-plasmonic phenomena to noble-metal/metal oxide systems in order to build up a solid knowledge base for the rational design of MP-NHs with predictable responses.

In this work we report on the investigation of colloidal Au@iron oxide core@shell MP-NHs characterized by a concentric flower-like topological profile, by using a combined experimental approach involving X-ray magnetic circular dichroism (XMCD) spectroscopy, X-ray absorption near-edge structure (XANES) spectroscopy, transmission electron microscopy (TEM), and SQUID magnetometry. Taking advantage of the atomic selectivity of the XMCD technique, for the first time we demonstrate the induction of magnetism into Au due to spin-polarization transfer from the magnetic iron oxide. The spin polarization was found to be dependent on the chemical and structural nature of the iron oxide domain with which the Au core domain was interfaced. Indeed, when iron was present in the lower bivalent oxidation state of magnetite and wustite, a synergistic behavior was observed, and a sizable magnetic moment on Au was detected. On the other hand, in the presence of trivalent iron of maghemite only, no signature of the interaction between the two moieties was identified. An increased hole density in the 5d states of the Au core suggested occurrence of a charge-transfer process concomitant to the spin-polarization transfer, which, in turn, originated from a direct hybridization between the Au 5d and Fe 3d states of the metallic core and oxide shell, respectively.

RESULTS AND DISCUSSION

To the purposes of our study, we compared two types of core@shell MP-NHs with different chemical composition and geometric parameters, henceforth referred to as samples S1 and S2. The MP-NHs samples were synthesized by an established surfactant-assisted seeded-growth technique.[2,16,40] The approach relied on performing heterogeneous nucleation and growth of iron oxide on pre-existing Au nanocrystals by manipulating the thermal decomposition of suitable iron precursors in 1-octadecene/oleil amine/oleic acid mixtures at 320 °C under N_2 atmosphere in the presence of preformed Au nanocrystal seeds that had been grown in a separate step.[16,40] The topology and relative Au and iron oxide domain sizes could be varied by selecting Au seeds with different dimensions and adjusting the relative seed to reactant ratio, according to known criteria.[2,16,21,22,40,41] After growth completion at high temperature, the crude reaction mixture was exposed to air for a short period at 80 °C. Postsynthesis processing of the MP-NHs (extraction, purification, redispersion, and storage in low-boiling nonpolar solvents) was entirely carried out using anhydrous solvents under inert atmosphere to prevent any further oxidation of the MP-NHs

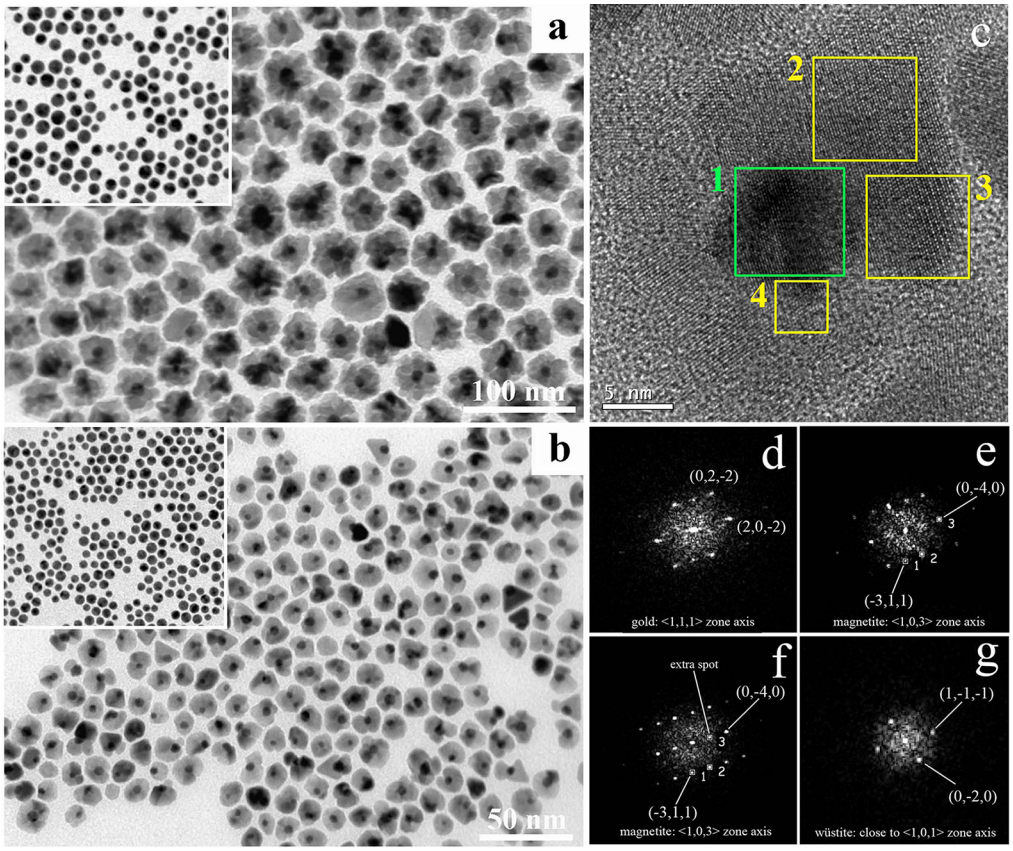

Figure 1. Representative low-magnification TEM images of colloidal MP-NHs with a Au@iron-oxide core@shell topology, referred to as sample S1 (a) and S2 (b) in the manuscript. The respective insets show the starting Au nanocrystal seeds. HRTEM image example of an individual core@shell MH-NH from sample S1 (c). Indexed FFTs (d−g) calculated for the corresponding regions enclosed by the square boxes labeled as 1, 2, 3, and 4 in panel c, respectively. In panel f, an extra spot (grain 3) due to the presence of an ordered defect structure in magnetite is marked.

(hence, changes in phase composition of their iron oxide component) prior to being characterized.

Figure 1 shows representative low-magnification transmission electron microscopy (TEM) pictures demonstrating the concentric core@shell geometry of the MP-NHs, in which the Au cores (corresponding to the starting seeds) exhibited a comparatively "darker" contrast due to their higher electron density and electron-diffracting power, relative to the surrounding iron oxide shell with variable shape profile. Sample S1 comprised objects made of *ca.* 8−10 nm Au cores enclosed within a multidomain, flower-like shell with an overall *ca.* 10−14 nm thickness (Figure 1a), while S2 contained MP-NHs made of ∼3 nm Au cores embedded within single-domain or multipetal shell with *ca.* 4−5 nm thickness (Figure 1b).

Figure 2a shows the XMCD spectrum of S1, taken at the L edge of Au. A magnetic dichroic signal was clearly detectable at both L_2 and L_3 edges, accounting for about 1% of the absorption at the L_3 edge. The field dependence of the XMCD measured at the L_3 edge of Au, 11930 eV was found to closely follow the SQUID magnetometric signal acquired on the same sample under identical conditions (inset in Figure 2a). As the intensity of the XMCD signal is proportional to the magnetic moment due to Au 5d states, the XMCD measurement indicated a direct electronic coupling between the Au and iron oxide moieties.

Since the magnetization reached full saturation below 6 T, the XMCD data for this sample could be used to separate the spin and angular parts of the Au magnetic moment. For randomly oriented nanoparticles the intra-atomic magnetic dipole moment averages out, and the sum rules used for extracting the spin and angular contribution to the total magnetic moment, m_{spin} and m_{orb}, respectively, are the following:[42,43]

$$m_{orb} = \frac{-2\langle A + B\rangle}{3C}\mu_B \quad (1)$$

$$m_{spin} = \frac{\langle -A + 2B\rangle}{C}\mu_B \quad (2)$$

with

$$C = \frac{\langle I_{L_3} + I_{L_2}\rangle}{N_h} \quad (3)$$

where A is the area of the L_3 XMCD peak, B is the area of the L_2 XMCD peak, I_{L_3} and I_{L_2} are the white-line integrated intensities after subtraction of the contributions

from the transitions to the continuum and N_h is the number of holes per atom in the *d* shell. Usually, the normalization constant *C* for Au is difficult to determine. In systems where the spin polarization is mainly due to interface effects, it is commonly assumed that *C* is transferable from compound to compound.[36] In line with this approach, the literature value $C = 7.8$[36] was used in eqs 1 and 2, yielding reasonable values for both m_{spin} and m_{orb}. In particular, we found $m_{orb} = 3.5 \times 10^{-3}$ and $m_{spin} = 8.7 \times 10^{-3}$ expressed in Bohr magneton units. It is, however, worth stressing that the ratio m_{orb}/m_{spin}, is, in any case, independent of the choice of the scaling constant. We found a value equal to 0.38, that is very high when compared to what has been documented in the literature for the Au L edges.[35,37,38,44,45] A quite large value for the orbital contribution (~30% of the total moment) has been recently reported to be associated with the induced paramagnetism in bulk Au; however, the actual value of the temperature-independent paramagnetic moment was found to be nearly 2 orders of magnitude smaller than the value extracted in this work.[34] Our result thus clarified that the intrinsic, small Pauli and orbital paramagnetism of Au could not be the at the origin of the magnetic moment of sample S1.

On the other hand, Figure 2b clarifies that no dichroism above the noise level at the Au L edges could be measured for sample S2. This observation indicated that the magnetic moment on Au in this sample, if any, should be below 10^{-5} Bohr magnetons. In addition, this result allowed excluding that XMCD on Au in S1 could otherwise originate from a Au_xFe_y alloy in the core of the MP-NHs, possibly formed upon Fe diffusion into the original Au nanocrystal seeds during the early stages of precursor/surfactant reaction at the Au surface. In fact, if this were the case, dichroism should have been observed for both samples.

The spin-polarization transfer from the iron oxide to Au domain is expected to be mainly an interface-driven phenomenon. However, since the percentage of Au atoms located at the interface was estimated to be less than 10% in S1 and around 50% in S2, the spin-polarization transfer should have been found to be more efficient for the latter sample if the interface extension were the dictating parameter, in contrast to our experimental evidence. Therefore, the different XMCD behavior observed should be instead related to the dissimilar chemical composition and/or structure of the magnetic domain in the respective cases. In order to support this hypothesis we further investigated the two samples by combining XANES, high-resolution TEM (HRTEM), and SQUID magnetometric measurements.

In Figure 3a the XANES spectra, recorded at the Fe−K edge of the two samples, are compared with those of bulk FeO (wüstite) and Fe_3O_4 (magnetite) used

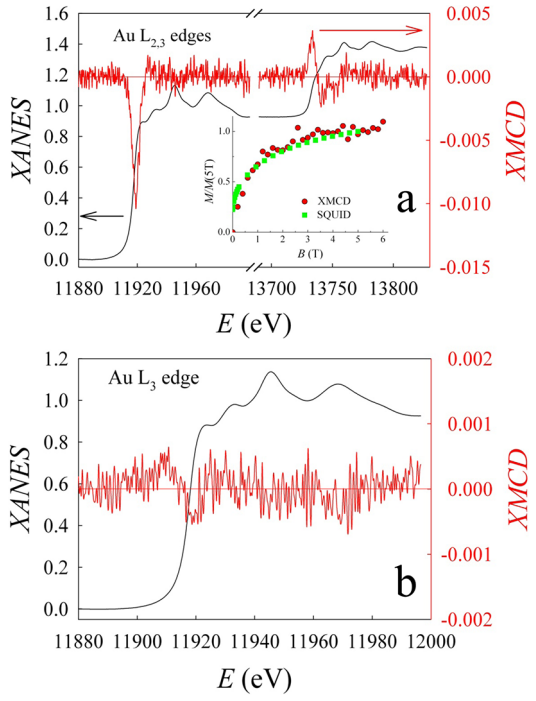

Figure 2. (a) XANES and XMCD spectra at the Au-$L_{2,3}$ edges, recorded at 7 K in an applied field of 7 T, for sample S1. The inset shows the variation of XMCD signal as a function of the field, measured at the minimum close to 11920 eV (red dots), along with the macroscopic magnetization curve (green dots); each curve is normalized to the corresponding value at 5 T. (b) XANES and XMCD spectra at the Au-L_3 edge for sample S2, recorded at 7 K in applied field of 7 T.

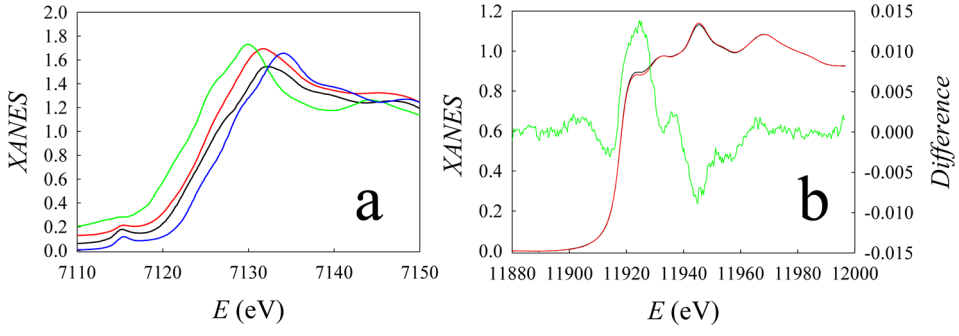

Figure 3. (a) Normalized Fe−K edge XANES spectra of sample S1, (red curve), S2, (blue), of bulk reference FeO (green), and Fe_3O_4 (black). For the sake of clarity the spectra have been shifted along the *y* axis. (b) Normalized Au-L_3 edges of the two nanoheterostructures, S1 (black) and S2, (red). The difference spectrum is shown as a green line.

as references. The spectra were collected in the same experimental conditions as those described above for the Au $L_{2,3}$ edge spectra. It is useful to recall here that XANES is a widely used and powerful tool for discriminating among different inorganic compounds: it can not only provide the spectral fingerprint of a given crystallographic phase, but also complementary information on the chemical nature of the sample, since the absorption edge position shifts toward lower energies with decreasing the average oxidation state of the photoabsorbing material. Our data thus confirmed that in the two samples Fe was present in different crystalline phases with dissimilar mean oxidation states. The shape of the Fe−K edge of S1 was found to closely resemble that of the mixed-valence Fe_3O_4 standard. However, the edge was located at a lower position in energy, thus indicating the presence of a higher amount of Fe ions in the divalent oxidation state. By fitting the edge feature with a linear combination of the FeO and Fe_3O_4 reference spectra, we inferred that FeO accounted for *ca.* 10% of the total Fe amount (atomic ratio) in sample S1.

HRTEM investigations, supported by fast Fourier transform (FFT) analysis of the image phase-contrast variation across individual nanocrystals, provided a deeper insight into the spatial distribution of the chemical composition and crystal phases in the heterostructures of sample S1. Representative results are illustrated in Figure 1c−g. The HRTEM image of a flower-like object (Figure 1c) confirmed the onion-like topology and revealed the existence of a central single-crystalline face-centered cubic Au core enclosed within a nearly continuous iron oxide shell. The symmetry of the Au diffraction pattern (Figure 1d) agreed with that expected for a truncated icosahedral geometry.[66] A close inspection of the heterostructure periphery clarified that the iron oxide shell incorporated several joint single-crystalline domains that could be univocally indexed to cubic magnetite (Figure 1e,f). As a consequence of the simultaneous nucleation and growth of multiple iron oxide "petals" on the various facets exposed by the original Au seeds, the magnetite sections appeared to be differently oriented relative to one another as well as to the primary electron beam. Changes in lattice contrast within individual magnetite domains pointed to the presence of defects. For example, while the FFT pattern corresponding to some domains matched well with that of pure magnetite (see, for instance, Figure 1e), the diffraction pattern relative to other sections showed the existence of additional planes with higher scattering power (see, for example, extra spots in Figure 1f), which could originate from ordered substitutional defects or impurities incorporated into the magnetite lattice. Finally, it is interesting to note that, while the shell was indeed dominated by the magnetite structure, small regions directly interfaced with the Au core exhibited a FFT pattern that satisfactorily matched with that of cubic wüstite (Figure 1g). The reduced number of diffraction spots observed, compared to those expected for the particular zone axis concerned, should be due to the limited area of the iron oxide region sampled for the FFT analysis and its subtle deviation from the exact alignment condition with respect to the primary electron beam.

The presence of wüstite in S1 can be justified by recalling the known mechanistic pathways that underlie the formation of iron/iron-oxide phases by surfactant-assisted thermal decomposition of iron carboxylates.[46−49] In the high-temperature synthesis stage, iron amino oleate complexes (formed by *in situ* reaction of $Fe(CO)_5$ or $Fe(acac)_3$ precursors and OLAC/OLAM surfactants) are decomposed to molecular monomer species (presumably, polyiron oxo clusters[47−49]) that can sustain the initial heterogeneous nucleation and growth of one or more reduced iron oxide phases, such as Fe_3O_4, FeO, and/or even of metallic Fe,[46−53] onto the Au seeds, due to the reducing environment offered by OLAM and trace amounts of CO and H_2 deriving from the pyrolysis reaction itself.[47] These iron-contaning phases, the relative proportions of which largely depend on the specific synthesis parameters,[46−53] can be subsequently converted to Fe_3O_4 and/or Fe_3O_4/γ-Fe_2O_3 (maghemite) mixtures upon controlled exposure to air or to a foreign organic oxidizer.[21,22,46−53] Given the low temperature (80 °C), short exposure time (1 h) and mild oxidizing conditions (atmospheric O_2 is poorly soluble in the nonpolar coordinating media in which the MP-NHs were grown) involved in the air-exposure step carried out in our syntheses, and considering the relatively large thickness of the iron oxide shell in S1, only partial conversion of the FeO domain to mixed-valence Fe_3O_4, rather than to fully oxidized γ-Fe_2O_3 phase, could be expected to occur, as actually detected by us. This result is consistent with the phase composition commonly assessed for iron oxide nanoparticles with sizes exceeding ~15 nm, prepared by analogous surfactant-assisted thermal decomposition of metal−organic precursors.[46−53] In addition, recent mechanistic studies on the development of FeO@Fe_3O_4 core@shell nanosystems,[46−49,52,53] suggest that FeO to Fe_3O_4 transformation in our Au@iron oxide MP-NHs should reasonably proceed *via* progressive oxidation from the surface of the FeO shell toward the interior. Accordingly, the residual FeO phase in our Au@iron oxide core@shell MP-NHs should be expected to be located in direct contact with the buried Au core, that is, far away from the outermost exposed surface region of the iron oxide shell section. Such topological picture is indeed in agreement with the HRTEM evidence acquired on sample S1.

On the other hand, as for what concerned sample S2 with the thinner iron oxide domain shell, the XANES edge energy was compatible with the presence of pure

Fe_2O_3. Furthermore, the spectral shape was consistent with the cubic spinel structure characteristic of γ-Fe_2O_3. This result is in line with the phase composition generally assessed for relatively small iron oxide nanoparticles, which are more chemically reactive and, consequently, predisposed to be fully oxidized.[46−50]

Figure 3b shows the XANES spectra of the two samples at the Au L_3 edge along with the corresponding difference spectrum. For both samples, the XANES manifold indicated the presence of Au in the metallic state. However, subtle differences were reliably detectable. Indeed, the region at around 11925 eV directly reflected the density of empty Au 5d states, which appeared to be higher for S1 than for S2, as evidenced in the difference spectrum. This was evidence for the existence of a larger density of holes in the Au 5d states in the former sample, which in turn was a signature of a higher degree of hybridization attained with the contiguous magnetic material in S1 with respect to S2. The electronic origin of this effect was further supported by the fact that changes in the spectral profile at higher energies reflected variations in the local chemical environment around Au. In this energy region the two samples showed very small differences, thus proving the fact that the local chemical environment of Au in the two samples was similar.

The macroscopic magnetic properties were investigated by recording the temperature dependence of the magnetization in a small 5 mT magnetic field after zero field (ZFC) and field cooling (FC) procedures. The temperature-dependent magnetization curves of S1 (Figure 4a) exhibited the typical features expected for weakly interacting single-domain magnetic nanoparticles, their magnetic moment being blocked at low temperature and free to fluctuate at room temperature (the blocking temperature was at *ca*. 250 K). The two steps at around 100 and 210 K in the ZFC curve are the signature of the Verwey transition, T_V, characteristic of Fe_3O_4 and of the antiferromagnetic ordering of the FeO phase (Néel temperature, $T_N \approx 200$ K), respectively.[54]

The ZFC/FC curves of S2 (Figure 4a) also showed evidence for a transition from a blocked to an unblocked regime with an average blocking temperature of around 180 K. The broad distribution of energy barriers can be justified on considering the irregular flower-like geometry of the magnetic shell domain, which can favor the occurrence of relaxation mechanisms different from the coherent rotation.[55] Unlike S1, no evidence for any structural or magnetic transition was observed in the ZFC/FC curves recorded for S2, confirming that the only iron oxide phase present in the shell was γ-Fe_2O_3. The different composition of the magnetic moiety of the two samples was further confirmed by the respective hysteresis loops recorded at 3 K (Figure 4b). While for S2 both the measured coercive field (40 mT) and the approach to saturation

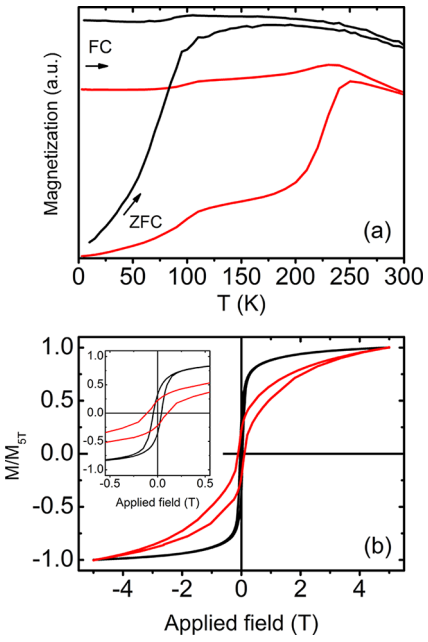

Figure 4. Temperature dependence of the magnetization (a) and hysteresis curve normalized at 5 T (b) for the two samples investigated; red and black curves refer to sample S1 and S2, respectively. The inset shows a magnified view of the low field region in the two loops in the low field region: colors are as in panels a and b.

were those typical of spinel ferrite nanoparticles, the presence of an antiferromagnetic phase (FeO) was clearly inferred for S1 from the higher coercivity (110 mT), the large irreversible field (up to 3 T), and the high-field slope of the magnetization curve.

To investigate the coupling between the two magnetic phases observed in S1 we recorded a hysteresis loop at 3 K after field cooling with a 5 T applied magnetic field from room temperature (above T_N of FeO). We observed a negative shift, $\mu_0 H_{Ex} = -124$ mT along the field axis and a 196 mT coercive field, $\mu_0 H_{Cex}$, which represents the fingerprint of an exchange-coupled antiferromagnetic/ferrimagnetic system.[56,57] However, in contrast to what is expected for conventional exchange-biased nanosystems, the phenomenon was also observed when the loop was recorded without cooling through any structural or magnetic (ordering, freezing, blocking, ...) transition. Indeed, after cooling from room temperature and applying the 5 T field at 100 K (below T_N but above T_V) we found $\mu_0 H_{Ex} = -86$ mT and $\mu_0 H_{Cex} = 167$ mT, while, on applying the same field at 40 K (below T_V), $\mu_0 H_{Ex}$ and $\mu_0 H_{Cex}$ were found to be −70 and 150 mT, respectively (Supporting Information, Figure S.I.-1). This behavior indicates that the mechanism of coupling between the two magnetic phases is much more complex than the simple spin pinning caused by uncompensated ferrimagnetic/antiferromagnetic interfaces, which typically is considered to be responsible for the shift of the field-cooled hysteresis loop. Work is in progress in order to better elucidate this unusual behavior.

Conversely, exchange bias was not observed in sample S2, confirming that it comprised only a single magnetic phase, in good agreement with information obtained by XANES (Supporting Information, Figure S.I.-2).

All experimental observations pointed out that the spin polarization transfer to Au atoms critically depended on the chemical composition of the magnetic phase neighbor. In particular, the presence of divalent Fe^{2+} ions appeared to be the stringent requirement for the insurgence of a magnetic moment on Au.

In previous studies the detection of a nonzero magnetic moment on Au in bimetallic systems was explained in terms of electronic hybridization between the valence bands of the two metals, with subsequent spin polarization transfer from the magnetic moiety.[35,37,38] The same phenomenon has also been reported for Ag in proximity of FeNi[56] and in Ag−Fe alloys[57] and discussed using similar arguments.

In the case of S1, the system was made dominantly of Fe_3O_4; this oxide is featured by a very low band gap (0.1 eV)[58] which leads to a metallic-like behavior. It is well-known that bulk stoichiometric Fe_3O_4 undergoes a metal to insulator transition at the Verwey temperature (120 K) associated with charge localization,[59,60] although the exact nature of this transition is still largely debated.[61] However, as far as nanometer-scale Fe_3O_4 domains are involved, a highly defective crystal structure can be expected, as indeed suggested by our HRTEM analyses. Defects can indeed be responsible for significant deviations from the bulk behavior, including the disappearance of the Verwey transition for small crystallites.[62] Furthermore in thin polycrystalline films, no discontinuity in the conductivity across T_V has been detected, despite the observed change in magnetic susceptibility.[63,64]

By taking into account the above arguments and the experimental hints gathered from the differences in the Au L_3 spectra shown in Figure 3b, for sample S1 we can postulate a mechanism reminiscent of that based on metal−metal hybridization in magneto-plasmonic alloy nanomaterials, which could explain the observed polarization transfer. Actually, the metal-to-insulator transition could be suppressed by the presence of Fe^{2+} ions in FeO strongly coupled to the Fe_3O_4 domains, which could modify the electronic structure of the system, thus preserving the electron hopping process responsible for the metallic-like behavior of magnetite. The very large value for the orbital part of the magnetic moment on the Au 5*d* states (m_{orb}/m_{spin} = 0.38) that was found for sample S1 is in agreement with a mechanism of spin-polarization transfer in which the hybridization between Au and Fe states should play a key role. On the other hand, the insulating nature of the γ-Fe_2O_3 shell surrounding the noble metal core in sample S2 is expected to prevent the spin-polarization transfer across the Au/oxide interface, in agreement with our experimental evidence.

CONCLUSION

In summary, we observed the insurgence of a magnetic moment in the Au 5d band of colloidal Au@iron oxide core@shell MP-NHs by using XMCD spectroscopy at the Au L edge and attributed it to a spin-polarization transfer from the magnetic oxide to the noble metal. This is, to the best of our knowledge, the first report of such an induced magnetic moment transferred from a transition-metal oxide to a nonmagnetic plasmonic metal. Moreover, we found that the chemical and structural nature of the magnetic phase (*i.e.*, either magnetite in combination with wüstite, or maghemite, as proven by XANES and magnetometric experiments) plays a key role in determining the onset of this phenomenon. Maghemite is, in fact, unable to promote any spin polarization transfer, in contrast to what magnetite can do. The different behavior was provisionally explained by invoking the half-metallic character of the latter oxide, which was preserved across T_V. Such character can give rise to a partial hybridization with the Au electronic states.

Further XMCD studies are certainly needed to gain a deeper understanding of the mechanism that accounts for the observed spin-transfer phenomenon. At present, it is difficult to envisage the generality of the proposed hybridization of Fe and Au states, and to explain its dependence on the morpholog, and geometry of a MP-NHs. Despite these limitations, here we have clearly shown that electron or charge transfer is a crucial prerequisite to attaining spin-transfer from magnetic iron oxide to plasmonic Au. In addition, the distinct behavior of the identified iron oxides in terms of spin and electronic interaction with the contiguous nanosized Au domain suggests some precious guidelines for the rational design of magnetic-plasmonic nanoheterostructures. By proper selection of the chemical composition and structure of the magnetic component in oxide-based MP-NHs, it should be possible to modulate the degree of interaction between the magnetic and SPR moieties, ultimately giving access to systems with unprecedented physical properties that could arise from a genuine synergistic interplay of the SPR and magnetic functionalities rather than from their merely additive combination. For instance, the coupling of free electrons of a plasmonic domain to the spin-unbalanced population of a magnetic section could give rise to magneto-plasmonic modes whose dependence on an external magnetic field may be enhanced over that achievable with the sole plasmonic moiety. This could boost dramatic improvements in the SPR-based refractometric signal and plasmon-based wave guiding.

On the other hand, the observed spin polarization on Au 5d states is expected to be accompanied by an opposite spin unbalance of the 4s electrons.[37] These electrons are responsible for the plasmon resonances, hence it is reasonable to postulate the existence of spin-unbalanced plasmon oscillations. The spin contribution to the SPR (spin-plasmonics) is a novel concept, which can be envisaged as a further development of magneto-plasmonics by joining photonics and spintronics in the same way as spintronics has stemmed from the encounter of spin-dependent transport phenomena and electronics.[65]

MATERIALS AND METHODS

Materials. Hydrogen tetrachloroaurate(III) hydrate ($HAuCl_4 \cdot H_2O$, 99.998%), iron pentacarbonyl ($Fe(CO)_5$, 98%), iron(III) acetylacetonate ($Fe(C_5H_7O_2)_3$ or $Fe(acac)_3$, 97%), oleic acid ($C_{17}H_{33}CO_2H$ or OLAC, 90%), oleyl amine ($C_{17}H_{33}NH_2$ or OLAM, 70%), and 1-octadecene ($C_{18}H_{36}$ or ODE, 90%), benzyl ether ($(C_6H_5CH_2)_2O$ or BE, >98%), and 1,2-hexadecanediol ($C_{16}H_{34}O_2$ or HE, 97%) were purchased from Aldrich. All solvents used were of analytical grade and purchased from Aldrich. All chemicals and solvents were used as received.

Colloidal Nanocrystal Synthesis. All syntheses were carried out using a standard Schlenk line setup. Stock solutions of $HAuCl_4$, OLAC, OLAC, and Au seeds in ODE or BE were prepared in a N_2-protected glovebox. Au nanocrystals were prepared by OLAM-driven reduction of $HAuCl_4$ in an ODE/OLAM mixture at 120−150 °C.[16] Au/iron oxide MP-NHs were synthesized at 300−320 °C by reacting either $Fe(CO)_5$ in ODE/OLAM/OLAC mixtures[16] or $Fe(acac)_3$ in BE/OLAM/OLAC/HE mixtures, respectively, which contained preformed size-controlled Au nanocrystal seeds, under nitrogen atmosphere, as described elsewhere.[16,32,40] To obtain MP-NHs with different domain sizes and topologies, the absolute concentrations of the Au seeds and iron precursor, and their relative ratio were varied. Following the high-temperature step, the heating source was removed, the reaction mixture was allowed to naturally cool down to 80 °C and was exposed to air for 1 h to allow stabilization of the degree of oxidation of the iron oxide component. After the synthesis, the MP-NHs were processed so as to prevent any further oxidation and, hence, changes in the iron-oxide phase composition. The MP-NHs were extracted from the crude reaction mixture upon flocculation induced by the addition of an anhydrous (oxygen-free) mixture 2-propanol/acetone under N_2 flow, separated by centrifugation, and then washed three times with acetone to remove any reactant residuals and unbound surfactants. The as-purified MP-NHs were rapidly dried under vacuum, then transferred to a N_2-protected glovebox and used to prepare stable colloidal solutions in anhydrous solvents ($CHCl_3$ or toluene) under N_2 atmosphere. Such MH-NH solutions were stored in the glovebox prior to further use and analyzed within a few days from the preparation.

Characterization Techniques. *Transmission Electron Microscopy (TEM).* Low-resolution TEM images were recorded with a Jeol Jem 1011 microscope operating at an accelerating voltage of 100 kV. Phase-contrast high-resolution TEM (HRTEM) experiments were performed using a Jeol 2010F UHR microscope operating at 200 keV. The objective lens had a spherical aberration coefficient of 0.47 ± 0.01 mm, allowing a resolution of 0.19 nm at optimum defocus in HRTEM imaging. Samples for analysis were prepared in a N_2-protected glovebox by dropping a dilute MP-NH solution onto carbon-coated copper grids, then allowing the solvent to evaporate. Finally, the grids were rapidly transferred to the microscope. The crystallographic parameters used for fast Fourier transform (FFT) analysis of HRTEM images were the following: space group $Fd\bar{3}m$, a = 8.396 Å, for Fe_3O_4; space group $P4_332$, a = 8.346 Å for γ-Fe_2O_3; space group $Fm\bar{3}m$, a = 4.307 Å for FeO; space group $Fm\bar{3}m$, a = 4.07 Å for Au.

X-ray Magnetic Circular Dichroism (XMCD) and X-ray Absorption Near-Edge Structure (XANES) Spectroscopy Measurements. Au-$L_{2,3}$ XMCD and Fe−K edge XANES spectra were collected at the ID12 beamline at the European Synchrotron Radiation Facility (ESRF, Grenoble, France) in fluorescence mode, under an applied magnetic field of ±6 T. Samples for the measurements were prepared by drop-casting concentrated MP-NH solutions in $CHCl_3$ onto the sample holder, then allowing the solvent to evaporate, and finally cooling down to 7 K. The degree of circular polarization was estimated to be 97%, therefore no correction for incomplete polarization was applied. Owing to the small amount of sample used in the XMCD measurements, no corrections for self-absorption were needed. The XMCD spectra were first collected by reversing the helicity of the incoming photon beam. Duplicate XMCD spectra were also recorded after reversing the direction of the applied field. This procedure was repeated up to eight times. Once the equivalence of field and helicity reversal had been checked, the spectra were averaged over all the scans for each direction of the field and helicity; then, the I^+ (I^-) absorption spectrum was obtained by averaging the right (left) and left (right) polarized spectra for both directions of the field. The spectra were normalized by fitting the pre-edge to a straight line and averaging the postedge to 1 for the L_3 edge, and to 0.45 for the L_3 edge. The XMCD signal was then defined as $I^+ - I^-$. The unpolarized spectra were obtained by averaging I^+ and I^-.

Magnetic Measurements. Magnetic measurements were performed using a Quantum Design MPMS SQUID magnetometer operating in the 1.8−350 K temperature range with applied field up to 5.0 T. Samples were obtained by depositing a few drops of the colloidal MP-NH solution onto a Teflon film in a glovebox and then rapidly transferring them into the magnetometer. All data were corrected for the diamagnetic contribution of the sample holder.

Conflict of Interest: The authors declare no competing financial interest.

Supporting Information Available: Dependence of exchange bias on the field cooling temperature of sample S1; low temperature field cooled hysteresis loop of sample S2. This material is available free of charge *via* the Internet at http://pubs.acs.org.

Acknowledgment. This work was funded by the Fondazione Cariplo through Project No. 2010-0612 "Chemical synthesis and characterization of magneto-plasmonic nano-heterostructures". ESRF is also acknowledged for provision of beamtime (Expt. HE-3431). V.V., P.D.C., and F.P. acknowledge partial financial support by the Italian Ministry of Education, University and Research through the project AEROCOMP (Contract MIUR No. DM48391), FIRB Project "Rete ItalNanoNet" (Contract MIUR RBPR05JH2P) and FIRB Futuro in Ricerca 2010 Project "NanoPlasMag" (Contract MIUR RBFR10OA10).

Note Added after ASAP Publication: After this paper was published online January 2, 2013, a correction was made to the affiliation for authors C.d.J.F. and C.S. The corrected version was reposted January 11, 2013.

REFERENCES AND NOTES

1. Burns, A.; Ow, H.; Wiesner, U. Fluorescent Core−Shell Silica Nanoparticles: Towards "Lab on a Particle" Architectures for Nanobiotechnology. *Chem. Soc. Rev.* **2006**, *35*, 1028–1042.
2. Carbone, L.; Cozzoli, P. D. Colloidal Heterostructured Nanocrystals: Synthesis and Growth Mechanisms. *Nano Today* **2010**, *5*, 449–493.
3. Cortie, M. B.; McDonagh, A. M. Synthesis and Optical Properties of Hybrid and Alloy Plasmonic Nanoparticles. *Chem. Rev.* **2011**, *111*, 3713–3735.

4. Chaudhuri, R. G.; Paria, S. Core/Shell Nanoparticles: Classes, Properties, Synthesis Mechanisms, Characterization, and Applications. *Chem. Rev.* **2012**, *112*, 2373–2433.
5. Armelles, G.; Cebollada, A.; García-Martín, A.; García-Martín, J. M.; González, M. U.; González-Díaz, J. B.; Ferreiro-Vila, E.; Torrado, J. F. Magnetoplasmonic Nanostructures: Systems Supporting Both Plasmonic and Magnetic Properties. *J. Opt. A: Pure Appl. Opt.* **2009**, *11*, 114023.
6. Leung, K. C.-F.; Xuan, S.; Zhu, X.; Wang, D.; Chak, C.-P.; Lee, S.-F.; Ho, W. K.-W.; Chung, B. C.-T. Gold and Iron Oxide Hybrid Nanocomposite Materials. *Chem. Soc. Rev.* **2012**, *41*, 1911–1928.
7. Wang, L.; Luo, J.; Maye, M. M.; Fan, Q.; Rendeng, Q.; Engelhard, M. H.; Wang, C.; Lin, Y.; Zhong, C.-J. Iron Oxide-Gold Core–Shell Nanoparticles and Thin Film Assembly. *J. Mater. Chem.* **2005**, *15*, 1821–1832.
8. Gu, H. W.; Yang, Z. M.; Gao, J. H.; Chang, C. K.; Xu, B. Heterodimers of Nanoparticles: Formation at a Liquid–Liquid Interface and Particle-Specific Surface Modification by Functional Molecules. *J. Am. Chem. Soc.* **2005**, *127*, 34–35.
9. Choi, J.-S.; Jun, Y.-W.; Jeon, S.-I.; Kim, H. C.; Shin, J.-S.; Cheon, J. Biocompatible Heterostructured Nanoparticles for Multimodal Biological Detection. *J. Am. Chem. Soc.* **2006**, *128*, 15982–15983.
10. Zhao, X.; Cai, Y.; Wang, T.; Shi, Y.; Jiang, G. Preparation of Alkanethiolate-Functionalized Core/Shell Fe_3O_4@Au Nanoparticles and Its Interaction with Several Typical Target Molecules. *Anal. Chem.* **2008**, *80*, 9091–9096.
11. Gao, J.; Gu, H.; Xu, B. Multifunctional Magnetic Nanoparticles: Design, Synthesis, and Biomedical Applications. *Acc. Chem. Res.* **2009**, *42*, 1097–1107.
12. Jiang, J.; Gu, H. W.; Shao, H. L.; Devlin, E.; Papaefthymiou, G. C.; Ying, J. Y. Bifunctional Fe_3O_4–Ag Heterodimer Nanoparticles for Two-Photon Fluorescence Imaging and Magnetic Manipulation. *Adv. Mater.* **2008**, *20*, 4403–4407.
13. Wang, L.; Bai, J.; Li, Y.; Huang, Y. Multifunctional Nanoparticles Displaying Magnetization and Near-IR Absorption. *Angew. Chem. Int Ed.* **2008**, *47*, 2439–2442.
14. Wei, Q.; Song, H.-M.; Leonov, A. P.; Hale, J. A.; Oh, D.; Ong, Q. K.; Ritchie, K.; Wei, A. Gyromagnetic Imaging: Dynamic Optical Contrast Using Gold Nanostars with Magnetic Cores. *J. Am. Chem. Soc.* **2009**, *131*, 9728–9734.
15. Li, Y.; Zhang, Q.; Nurmikko, A. V.; Sun, S. Enhanced Magnetooptical Response in Dumbbell-like Ag–$CoFe_2O_4$ Nanoparticle Pairs. *Nano Lett.* **2005**, *5*, 1689–1692.
16. Yu, H.; Chen, M.; Rice, P. M.; Wang, S. X.; White, R. L.; Sun, S. Dumbbell-like Bifunctional Au–Fe_3O_4 Nanoparticles. *Nano Lett.* **2005**, *5*, 379–382.
17. Tomita, S.; Kato, T.; Tsunashima, S.; Iwata, S.; Fujii, M.; Hayashi, S. Magneto-optical Kerr Effects of Yttrium–Iron Garnet Thin Films Incorporating Gold Nanoparticles. *Phys. Rev. Lett.* **2006**, *96*, 167402.
18. Xu, Z.; Hou, Y.; Sun, S. Magnetic Core/Shell Fe_3O_4/Au and Fe_3O_4/Au/Ag Nanoparticles with Tunable Plasmonic Properties. *J. Am. Chem. Soc.* **2007**, *129*, 8698–8699.
19. González-Diaz, J. B.; García-Martín, A.; García-Martín, J. M.; Cebollada, A.; Armelles, G.; Sepúlveda, B.; Alaverdyan, Y.; Käll, M. Plasmonic Au/Co/Au Nanosandwiches with Enhanced Magneto-optical Activity. *Small* **2008**, *4*, 202–205.
20. Levin, C. S.; Hofmann, C.; Ali, T. A.; Kelly, A. T.; Morosan, E.; Nordlander, P.; Whitmire, K. H.; Halas, N. J. Magnetic–Plasmonic Core–Shell Nanoparticles. *ACS Nano* **2009**, *3*, 1379–1388.
21. Wang, C.; Xu, C.; Zeng, H.; Sun, S. Recent Progress in Syntheses and Applications of Dumbbell-like Nanoparticles. *Adv. Mater.* **2009**, *21*, 3045–3052.
22. Lee, Y.; Garcia, M. A.; Frey Huls, N. A; Sun, S. Synthetic Tuning of the Catalytic Properties of Au–Fe_3O_4 Nanoparticles. *Angew. Chem., Int. Ed.* **2010**, *49*, 1271–1274.
23. Jain, P. K.; Xiao, Y.; Walsworth, R.; Cohen, A. E. Surface Plasmon Resonance Enhanced Magneto-optics (SuPREMO): Faraday Rotation Enhancement in Gold-Coated Iron Oxide Nanocrystals. *Nano Lett.* **2009**, *9*, 1644–1650.
24. Temnov, V. V.; Armelles, G.; Woggon, U.; Guzatov, D.; Cebollada, A.; García-Martín, A.; García-Martín, J. M.; Thomay, T.; Leitenstorfer, A.; Bratschitsch, R. Active Magneto-Plasmonics in Hybrid Metal–Ferromagnet Structures. *Nat. Photon.* **2010**, *4*, 107–111.
25. Bogani, L.; Cavigli, L.; de Julián Fernández, C.; Mazzoldi, P.; Mattei, G.; Gurioli, M.; Dressel, M.; Gatteschi, D. Photocoercivity of Nano-stabilized Au: Fe Superparamagnetic Nanoparticles. *Adv. Mater.* **2010**, *22*, 4054–4058.
26. Wang, L.; Clavero, C.; Huba, Z.; Carroll, K. J.; Carpenter, E. E.; Gu, D.; Lukaszew, R. A. Plasmonics and Enhanced Magneto-optics in Core–Shell Co–Ag Nanoparticles. *Nano Lett.* **2011**, *11*, 1237–1240.
27. Bonanni, V.; Bonetti, S.; Pakizeh, T.; Pirzadeh, Z.; Chen, J.; Nogués, J.; Vavassori, P.; Hillenbrand, R.; Åkerman, J.; Dmitriev, A. Designer Magnetoplasmonics with Nickel Nanoferromagnets. *Nano Lett.* **2011**, *11*, 5333–5338.
28. Ferreiro-Vila, E.; Iglesias, M.; Paz, E.; Palomares, F. J.; Cebollada, F.; González, J. M.; Armelles, G.; García-Martín, J. M.; Cebollada, A. Magneto-Optical and Magnetoplasmonic Properties of Epitaxial and Polycrystalline Au/Fe/Au Trilayers. *Phys. Rev. B* **2011**, *83*, 205120.
29. Korobchevskaya, K.; George, C.; Diaspro, A.; Manna, L.; Cingolani, R.; Comin, A. Ultrafast Carrier Dynamics in Gold/Iron-Oxide Nanocrystal Heterodimers. *Appl. Phys. Lett.* **2011**, *99*, 011907.
30. Belotelov, V. I.; Akimov, I. A.; Pohl, M.; Kotov, V. A.; Kasture, S.; Vengurlekar, A. S.; Gopal, A. V.; Yakovlev, D. R.; Zvezdin, A. K.; Bayer, M. Enhanced Magneto-optical Effects in Magnetoplasmonic Crystals. *Nat. Nanotechnol.* **2011**, *6*, 370–376.
31. Comin, A.; Korobchevskaya, K.; George, C.; Diaspro, A.; Manna, L. Plasmon Bleaching Dynamics in Colloidal Gold-Iron Oxide Nanocrystal Heterodimers. *Nano Lett.* **2012**, *12*, 921–926.
32. Umut, E.; Pineider, F.; Arosio, P.; Sangregorio, C.; Corti, M.; Tabak, F.; Lascialfari, A.; Ghigna, P. Magnetic, Optical and Relaxometric Properties of Organically Coated Gold–Magnetite (Au–Fe_3O_4) Hybrid Nanoparticles for Potential Use in Biomedical Applications. *J. Magn. Magn. Mater.* **2012**, *324*, 2373–2379.
33. Frey, N. A.; Srinath, S.; Srikanth, H.; Wang, C.; Sun, S. Static and Dynamic Magnetic Properties of Composite Au–Fe_3O_4 Nanoparticles. *IEEE Trans. Magn.* **2007**, *43*, 3094–3096.
34. Suzuki, M.; Kawamura, N.; Miyagawa, H.; Garitaonandia, J. S.; Yamamoto, Y.; Hori, H. Measurement of a Pauli and Orbital Paramagnetic State in Bulk Gold Using X-ray Magnetic Circular Dichroism Spectroscopy. *Phys. Rev. Lett.* **2012**, *108*, 047201 1–5.
35. Wilhelm, F.; Angelakeris, M.; Jaouen, N.; Poulopoulos, P.; Papaioannou, E. Th.; Mueller, Ch.; Fumagalli, P.; Rogalev, A.; Flevaris, N. K. Magnetic Moment of Au at Au/Co Interfaces: A Direct Experimental Determination. *Phys. Rev. B* **2004**, *69*, 220404 1–4.
36. Bartolomé, J.; García, L. M.; Bartolomé, F.; Luis, F.; López-Ruiz, R.; Petroff, F.; Deranlot, C.; Wilhelm, F.; Rogalev, A.; Bencok, P.; *et al*. Magnetic Polarization of Noble Metals by Co Nanoparticles in M-Capped Granular Multilayers (M = Cu, Ag, and Au): An X-ray Magnetic Circular Dichroism Study. *Phys. Rev. B* **2008**, *77*, 184420 1–12.
37. Wilhelm, F.; Poulopoulos, P.; Kapaklis, V.; Kappler, J.-P.; Jaouen, N.; Rogalev, A.; Yaresko, A. N.; Politis, C. Au and Fe Magnetic Moments in Disordered Au–Fe Alloys. *Phys. Rev. B* **2008**, *77*, 224414 1–6.
38. de Julián Fernández, C.; Mattei, G.; Paz, E.; Novak, R. L.; Cavigli, L.; Bogani, L.; Palomares, F. J.; Mazzoldi, P.; Caneschi, A. Coupling between Magnetic and Optical Properties of Stable Au–Fe Solid Solution Nanoparticles. *Nanotechnology* **2010**, *21*, 165701.
39. Casavola, M.; Buonsanti, R.; Caputo, G.; Cozzoli, P. D. Colloidal Strategies for Preparing Oxide-Based Hybrid Nanocrystals. *Eur. J. Inorg. Chem.* **2008**, 837–854.
40. Shi, W.; Zeng, H.; Sahoo, Y.; Ohulchanskyy, T. Y.; Ding, Y.; Wang, Z. L.; Swihart, M. T.; Prasad, P. N. A General Approach to Binary and Ternary Hybrid Nanocrystals. *Nano Lett.* **2006**, *6*, 875–881.

41. Wei, Y.; Klajn, R.; Pinchuk, A. O.; Grzybowski, B. A. Synthesis, Shape Control, and Optical Properties of Hybrid Au/Fe_3O_4 "Nanoflowers. *Small* **2008**, *4*, 1635–1639.
42. Thole, B. T.; Carra, P.; Sette, F.; van der Laan, G. X-Ray Circular Dichroism as a Probe of Orbital Magnetization. *Phys. Rev. Lett.* **1992**, *68*, 1943–1946.
43. Carra, P.; Thole, B. T.; Altarelli, M.; Wang, X. X-ray Circular Dichroism and Local Magnetic Fields. *Phys. Rev. Lett.* **1993**, *70*, 694–697.
44. Yamamoto, Y.; Miura, T.; Suzuki, M.; Kawamura, N.; Miyagawa, H.; Nakamura, T.; Kobayashi, K.; Teranishi, T.; Hori, H. Direct Observation of Ferromagnetic Spin Polarization in Gold Nanoparticles. *Phys. Rev. Lett.* **2004**, *93*, 116801 1–4.
45. de la Venta, J.; Bouzas, V.; Pucci, A.; Laguna-Marco, M. A.; Haskel, D.; te Velthuis, S. G. E.; Hoffmann, A.; Lal, J.; Bleuel, M.; *et al.* X-ray Magnetic Circular Dichroism and Small Angle Neutron Scattering Studies of Thiol Capped Gold Nanoparticles. *J. Nanosci. Nanotechnol.* **2009**, *9*, 6434–6438.
46. Park, J.; An, K.; Hwang, Y.; Park, J.-G.; Noh, H.-J.; Kim, J.-Y.; Park, J.-H.; Hwang, N.-M.; Hyeon, T. Ultra-large-scale Synthesis of Monodisperse Nanocrystals. *Nat. Mater.* **2004**, *3*, 891–895.
47. Kwon, S. G.; Piao, Y.; Park, J.; Angappane, S.; Jo, Y.; Hwang, N.-M.; Park, J.-G.; Hyeon, T. Kinetics of Monodisperse Iron Oxide Nanocrystal Formation by "Heating-up" Processs. *J. Am. Chem. Soc.* **2007**, *129*, 12571–12584.
48. Kwon, S. G.; Hyeon, T. Kinetics of Monodisperse Iron Oxide Nanocrystal Formation by "Heating-up" Process. *Acc. Chem. Res.* **2008**, *41*, 1696–1709.
49. Shavel, A.; Rodríguez-González, B.; Spasova, M.; Farle, M.; Liz-Marzán, L. M. Synthesis and Characterization of Iron/Iron Oxide Core/Shell Nanocubes. *Adv. Funct. Mater.* **2007**, *17*, 3870–3876.
50. Chen, C.-J.; Chiang, R.-K.; Lai, H.-Y.; Lin, C.-R. Characterization of Monodisperse Wüstite Nanoparticles Following Partial Oxidation. *J. Phys. Chem. C* **2010**, *114*, 4258–4263.
51. Pichon, B. P.; Gerber, O.; Lefevre, C.; Florea, I.; Fleutot, S.; Baaziz, W.; Pauly, M.; Ohlmann, M.; Ulhaq, C.; Ersen, O.; *et al.* Microstructural and Magnetic Investigations of Wüstite-Spinel Core−Shell Cubic-Shaped Nanoparticles. *Chem. Mater.* **2011**, *23*, 2886–2900.
52. Corrias, A.; Mountjoy, G.; Loche, D.; Puntes, V.; Falqui, A.; Zanella, M.; Parak, W. J.; Casula, M. F. Identifying Spinel Phases in Nearly Monodisperse Iron Oxide Colloidal Nanocrystal. *J. Phys. Chem. C* **2009**, *113*, 18667–18675.
53. Casula, M. F.; Jun, Y. W.; Zaziski, D. J.; Chan, E. M.; Corrias, A.; Alivisatos, A. P. The concept of delayed Nucleation in Nanocrystal Growth Demonstrated for the Case of Iron Oxide Nanodisks. *J. Am. Chem. Soc.* **2006**, *128*, 1675–1682.
54. Coey, J. M. D. *Magnetism and Magnetic Materials*; Cambridge University Press: Cambridge, 2010; p 417−422.
55. Cabot, A.; Alivisatos, A. P.; Puntes, V. F.; Balcells, L.; Iglesias, O.; Labarta, A. Magnetic Domains and Surface Effects in Hollow Maghemite Nanoparticles. *Phys. Rev. B* **2009**, *79*, 094419 1–7.
56. Jaouen, N.; Wilhelm, F.; Rogalev, A.; Goulon, J.; Ortega, L.; Tonnerre, J. M.; Yaresko, A. Electronic and Magnetic Interfacial States of Ag in an $Ni_{81}Fe_{19}$/Ag Coupled Multilayer. *J. Phys.: Condens. Matter* **2008**, *20*, 095005.
57. Alonso, J.; Fernández-Gubieda, M. L.; Sarmiento, G.; Chaboy, J.; Boada, R.; García Prieto, A.; Haskel, D.; Laguna-Marco, M. A.; Lang, J. C.; Meneghini, C.; *et al.* Interfacial Magnetic Coupling between Fe Nanoparticles in Fe−Ag Granular Alloys. *Nanotechnology* **2012**, *23*, 025705.
58. Cornell, R. M.; Schwertmann, U. *The Iron Oxides*; VCH: Weinheim, Germany, 1996.
59. García, J.; Subías, G. The Verwey Transition—A New Perspective. *J. Phys.: Condens. Matter* **2004**, *16*, R145–R178.
60. Walz, F. The Verwey Transition−A Topical Review. *J. Phys.: Condens. Matter* **2002**, *14*, R285–R340.
61. Senn, M. S.; Wright, J. P.; Attfield, J. P. Charge Order and Three-Site Distortions in the Verwey Structure of Magnetite. *Nature* **2011**, *481*, 173–176.
62. Goya, G. F.; Berquo, T. S.; Fonseca, F. C.; Morales, M. P. Static and Dynamic Magnetic Properties of Spherical Magnetite Nanoparticles. *J. Appl. Phys.* **2003**, *94*, 3520–3528.
63. Wang, L.; Li, J.; Ding, W.; Zhou, T.; Liu, B.; Zhong, W.; Wu, J.; Du, Y. Magnetoelectric Transport Properties of Quenched Polycrystalline Magnetite. *J. Magn. Magn. Mater.* **1999**, *207*, 111–117.
64. Li, X. W.; Gupta, A.; Xiao, G.; Gong, G. Q. Transport and Magnetic Properties of Epitaxial and Polycrystalline Magnetite Thin Films. *J. Appl. Phys.* **1998**, *83*, 7049–7051.
65. Chau, K. J.; Johnson, K. J.; Elezzabi, A. Y. Electron-Spin-Dependent Terahertz Light Transport in Spintronic-Plasmonic Media. *Phys. Rev. Lett.* **2007**, *98*, 133901.
66. Ascencio, J. A.; Perez, M.; Jose-Yacaman, M. A. Truncated Icosahedral Structure Observed in Gold Nanoparticles. *Surf. Sci.* **2000**, *447*, 73–80.